JOURNAL OF GEOPHYSICAL RESEARCH, VOL. 112, B02206, doi:10.1029/2006JB004689, 2007

Hydrothermal fluid flow and deformation in large calderas: Inferences from numerical simulations

Shaul Hurwitz,[1] Lizet B. Christiansen,[1] and Paul A. Hsieh[1]

Received 10 September 2006; revised 5 October 2006; accepted 17 October 2006; published 24 February 2007.

[1] Inflation and deflation of large calderas is traditionally interpreted as being induced by volume change of a discrete source embedded in an elastic or viscoelastic half-space, though it has also been suggested that hydrothermal fluids may play a role. To test the latter hypothesis, we carry out numerical simulations of hydrothermal fluid flow and poroelastic deformation in calderas by coupling two numerical codes: (1) TOUGH2 [Pruess et al., 1999], which simulates flow in porous or fractured media, and (2) BIOT2 [Hsieh, 1996], which simulates fluid flow and deformation in a linearly elastic porous medium. In the simulations, high-temperature water (350°C) is injected at variable rates into a cylinder (radius 50 km, height 3–5 km). A sensitivity analysis indicates that small differences in the values of permeability and its anisotropy, the depth and rate of hydrothermal injection, and the values of the shear modulus may lead to significant variations in the magnitude, rate, and geometry of ground surface displacement, or uplift. Some of the simulated uplift rates are similar to observed uplift rates in large calderas, suggesting that the injection of aqueous fluids into the shallow crust may explain some of the deformation observed in calderas.

Citation: Hurwitz, S., L. B. Christiansen, and P. A. Hsieh (2007), Hydrothermal fluid flow and deformation in large calderas: Inferences from numerical simulations, *J. Geophys. Res.*, *112*, B02206, doi:10.1029/2006JB004689.

1. Introduction

[2] Calderas are large, quasi-circular volcanic depressions, ranging up to 75 kilometers in the largest dimension, that form by roof collapse over an underlying shallow magma reservoir [*Lipman*, 1984, 1997]. The larger calderas (>5 km in diameter) are usually associated with cataclysmic ignimbrite eruptions in which magmatic volumes of at least several cubic kilometers are ejected [*Lipman*, 1997, 2000]. Sixteen large caldera forming eruptions have occurred in the Quaternary, of which the largest occurred at 760 ka, forming the Long Valley Caldera in California, 640 ka, forming the Yellowstone Caldera in Wyoming, and 75 ka, forming the Toba Caldera in Indonesia [*Lipman*, 2000].

[3] Most Quaternary calderas are characterized by periods of unrest at various timescales that are manifested by some combination of intense thermal activity, gas emissions, seismicity, and ground surface displacements (GSD) [*Newhall and Dzurisin*, 1988]. GSD rates in calderas range over several orders of magnitude (Table 1) and those detectable with modern geodetic techniques (e.g., trilateration, electronic distance meters, interferometric synthetic aperture radar, and GPS) are of special interest, because they are often interpreted as indicators of recent magma intrusion into the shallow crust [*Dvorak and Dzurisin*, 1997; *Dzurisin*, 2003; *Poland et al.*, 2006; *Wicks et al.*, 2006]. However, most reported GSD have not culminated in magma eruption, and eruptions can occur without significant GSD [*Pritchard and Simons*, 2002].

[4] Interpretations of GSD usually invoke volume change of a discrete source (often assumed to be a magma chamber) with a specified geometry in a homogeneous, isotropic, and elastic [*Mogi*, 1958; *Walsh and Decker*, 1971; *Vasco et al.*, 1988; *Yang et al.*, 1988; *Fialko et al.*, 2001], or viscoelastic [*Bonafede et al.*, 1986; *Newman et al.*, 2001] half-space. The calculated depth, shape, and volume change of the source in these models are derived from inversion of measured GSD. In many cases, observed surface displacements display a multifaceted pattern, implying that the magma plumbing system has a complex geometry that can only be modeled using a number of superimposed sources. In these circumstances, determination of the source parameters (e.g., depth, shape, volume change) is a nonunique problem.

[5] Such models cannot distinguish between an aqueous, low-density, low-viscosity fluid and a dense and viscous magma. Further, an increasing number of observations indicate a causal link between transient groundwater and/or gas pressures and GSD in calderas [*Dzurisin et al.*, 1990; *Bonafede*, 1991; *Wicks et al.*, 1998; *De Natale et al.*, 2001; *Chiodini et al.*, 2003; *Battaglia et al.*, 2006]. This suggests that a poroelastic approach, coupling fluid and solid stresses, to modeling GSD in calderas should be considered. Despite the growing number of suggestive observations, the interplay between groundwater flow dynamics and crustal mechanics in active calderas is poorly understood. In this study, we carry out numerical simulations of caldera hydrothermal systems with a goal of determining the range of

[1]U.S. Geological Survey, Menlo Park, California, USA.

Table 1. Documented Examples of Vertical Ground Surface Displacements in Large Calderas

Caldera	Period	Vertical Displacement Rate, mm/yr	Radius of Deformed Area, km	Comments	Reference
		Millennial and Centennial Displacements Based on Mapping			
Campi Flegrei	150 B.C. to 394	−14	6	Rapid uplift terminated by the 1538 Monte Nuovo eruption	*Orsi et al.* [1999] and *Morhange et al.* [2006]
	1450–1538	+102			
	1538–1905	−17			
Iwo Jima	1539–1988	+250		Uplift of the entire island Caldera displacements are unknown	*Newhall et al.* [1998]
Yellowstone	16–3 ka	−2	20–25	Secular trend of subsidence episodically interrupted by uplift	*Pierce et al.* [2002]
		Subannual to Decadal Displacements Based on Geodetic Measurements			
Aniakachak	1992–200	−13	5		*Kwoun et al.* [2006]
Campi Flegrei	1905–1968	−14	8	Secular trend of subsidence episodically interrupted by uplift	*Orsi et al.* [1999], *De Natale et al.* [2001], and *Beauducel et al.* [2004]
	1969–1972	+510			
	1972–1975	−70			
	1982–1984	+510			
	1985–1988	−50			
	1988–1989	+130			
Iwo Jima	1977–1995	−30	5	Concurrent with the island uplifting at a rate of 165 mm/yr	*Ukawa et al.* [2006]
Long Valley	1976–1980	+60	5	Displacement of the resurgent dome	*Langbein* [2003]
	1980–1983	+60			
	1988–1992	+18			
	1997–1998	+100			
	1998–2002	−5			
Rabaul	1971–1983	+115	5		*McKee et al.* [1984] and *Archbold et al.* [1988]
	1983–1985	+200			
Taupo	1979–1983	−2–10	12		*Otway et al.* [2002]
	1983–1984	+60			
	1984–1996	−5–11			
	1996–1999	+40			
Yellowstone	1923, 1975–1977	+14	20–25		*Pelton and Smith* [1979], *Wicks et al.* [1998], and *Dzurisin et al.* [1999]
	1976–1984	+22			
	1985–1995	−19			

plausible conditions under which poroelastic-induced GSD may occur.

2. Conceptual Model

[6] Following a widely accepted model of volcano hydrothermal systems [*Fournier*, 1999], we envision a caldera with a near-hydrostatic pressure distribution down to a brittle-ductile transition zone where the temperature is 350–450°C (Figure 1). Below the brittle-ductile transition zone there is a decrease in permeability and pressures are near lithostatic.

[7] Aqueous fluids and gas derived from crystallizing or convecting magma, or from episodic dike intrusion into crystallizing magma, are injected into the base of the hydrothermal system [*Fournier*, 1999]. Injection of high-temperature magmatic fluid into the shallow hydrothermal system can induce fluid overpressures that cause the host rocks to inflate by an amount controlled in part by the rigidity of the rock. Heating and thermal expansion of the saturated host rock also contributes to the inflation.

[8] In this conceptual model, subsidence can result from either a decrease in the flux of magmatic fluid entering the hydrothermal system or in response to rapid permeability increases that may occur when the pore pressures exceed the critical yield strength of the host rocks.

3. Numerical Methods

[9] To simulate poroelastic effects of magmatic fluid injection into the shallow hydrothermal system, we couple two numerical codes: (1) TOUGH2 [*Pruess et al.*, 1999], a

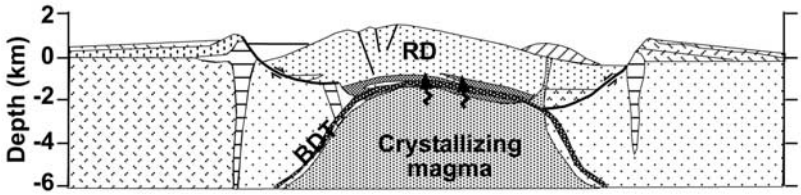

Figure 1. Conceptual model of a caldera [after *Lipman*, 1984] which includes the boundary faults and a resurgent dome (RD). The brittle-ductile transition (BDT) coincides with a transition from lithostatic (below) to hydrostatic (above) pressure distribution (following *Fournier* [1999]). The arrows represent fluid derived from magma crystallization, being injected into the base of the hydrothermal system.

three-dimensional (3-D) integrated finite difference simulator for nonisothermal, multicomponent and multiphase flow in porous or fractured media and (2) BIOT2 [*Hsieh*, 1996], which simulates axisymmetric or plane strain deformation and fluid flow in a linearly elastic porous medium. We selected TOUGH2 as the flow simulator because (1) it is a widely used public domain code; (2) it can simulate multiphase and multicomponent (H_2O-CO_2-NaCl) fluid flow, enabling future simulations to examine these effects, and (3) it allows for complex geometries, so that future simulations can incorporate effects of topography. BIOT2 is in the public domain, facilitating widespread use and verification of the coupled model.

Table 2. Summary of Numerical Simulations and the Variable Parameters

Simulation	k_x, m^2	k_x/k_z	Porosity	Injection Rate, t/d	Height of Cylinder, km	Heat Flux, mW/m^2	Shear Modulus, GPa
REFER	1×10^{-15}	1	0.10	2,000	5	100	1
Series A, Varying Injection Rate							
INJ-200	1×10^{-15}	1	0.10	200	5	100	1
INJ-5000	1×10^{-15}	1	0.10	10,000	5	100	1
INJ-10000	1×10^{-15}	1	0.10	20,000	5	100	1
Series B, Varying Injection Source Depth							
DEPTH-3	1×10^{-15}	1	0.10	2,000	3	100	1
DEPTH-4	1×10^{-15}	1	0.10	2,000	4	100	1
DEPTH-6	1×10^{-15}	1	0.10	2,000	6	100	1
DEPTH-7	1×10^{-15}	1	0.10	2,000	7	100	1
Series C, Varying Permeability							
PERM-17	1×10^{-17}	1	0.10	2,000	5	100	1
PERM-16	1×10^{-16}	1	0.10	2,000	5	100	1
PERM-14	1×10^{-14}	1	0.10	2,000	5	100	1
PERM-13	1×10^{-13}	1	0.10	2,000	5	100	1
Series D, Varying Anisotropic Permeability							
ANIS-10	1×10^{-15}	10	0.10	2,000	5	100	1
ANIS-100	1×10^{-15}	100	0.10	2,000	5	100	1
Series E, Varying Basal Heat Flux							
FLUX-150	1×10^{-15}	1	0.10	2,000	5	150	1
FLUX-200	1×10^{-15}	1	0.10	2,000	5	200	1
Series F, Varying Shear Modulus							
SHEAR-1	1×10^{-15}	1	0.10	2,000	5	100	0.1
SHEAR-10	1×10^{-15}	1	0.10	2,000	5	100	10
SHEAR-30	1×10^{-15}	1	0.10	2,000	5	100	30
Series G, Varying Porosity							
PORO-5	1×10^{-15}	1	0.05	2,000	5	100	1
PORO-20	1×10^{-15}	1	0.20	2,000	5	100	1
PORO-25	1×10^{-15}	1	0.25	2,000	5	100	1
Series H, Comparison With Observed Displacements in Campi Flegrei and Long Valley							
CYCL-INJ	1×10^{-16}	1	0.10	0–2,000	5	100	1
CYCL-PERM	1×10^{-15}–1×10^{-14}	1	0.10	2,000	3	100	1
Series I, Comparison With Observed Displacements in Campi Flegrei and Long Valley							
CF-3 km	1×10^{-15}	1	0.10	20,000	3	100	1
LVC-5 km	1×10^{-16}	1	0.10	4,000	5	100	1
LVC-8 km	8×10^{-17}	1	0.10	8,000	8	100	1

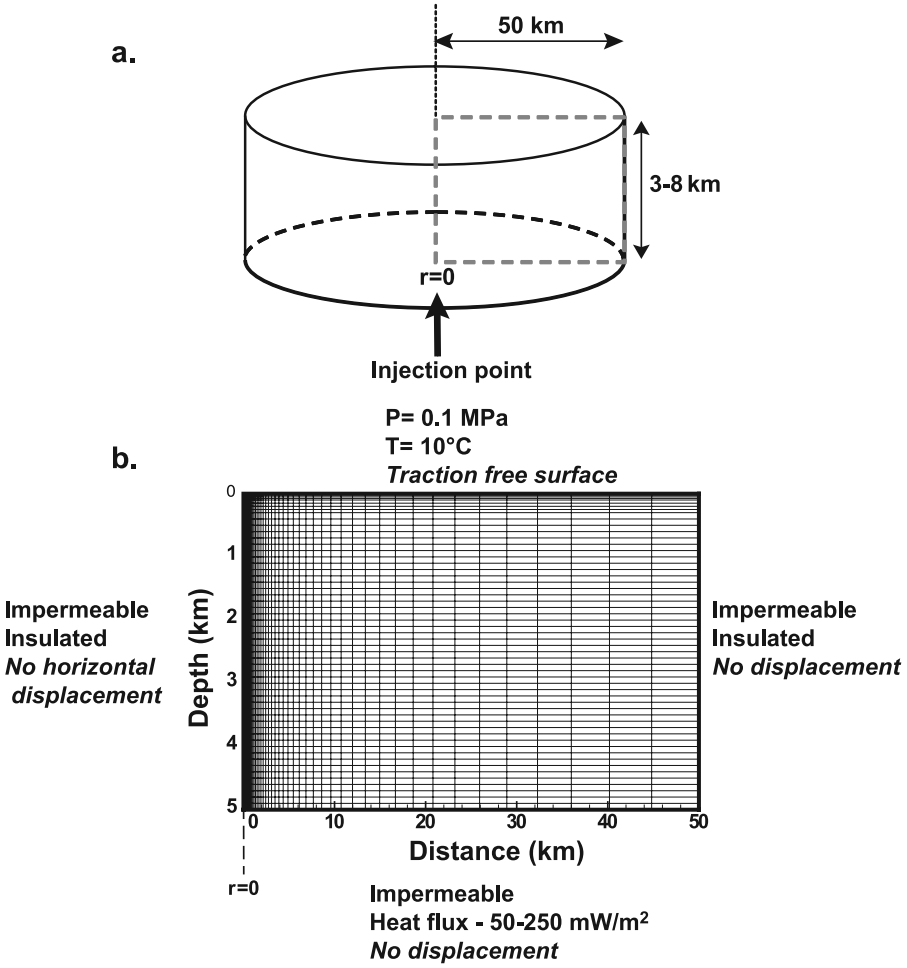

Figure 2. (a) Model domain showing the location of fluid injection and a slice through the cylindrical domain (rectangle with dashed gray boundaries) on which the computational grid was constructed and (b) computational grid for TOUGH2 and BIOT2 simulations. Boundary conditions for BIOT2 simulations are in italics.

[10] Fluid flow in the coupled simulator is modeled by TOUGH2 by solving a set of governing equations describing the conservation of mass, energy, and momentum. The compressibility of water is internally coded in TOUGH2 and varies with temperature and pressure. Detailed formulation of these equations can be found elsewhere [*Pruess et al.*, 1999]. BIOT2 is used to simulate poroelastic deformation of the host rock.

[11] In our simulations, both codes have the same computational mesh. However, the variables in TOUGH2 are defined at element centroids, whereas the variables in BIOT2 are defined at element corners. For each time step, the temperature and pressure at element centroids are calculated by TOUGH2. The values of pressure and temperature are interpolated to element corners, and then fed into BIOT2, where the displacement vector u is calculated for each node by solving

$$G\nabla^2 \mathrm{u} + \frac{G}{1-2\nu}\nabla(\nabla\cdot\mathrm{u}) - \nabla(p-p_0) - \frac{2G(1+\nu)\alpha}{3(1-2\nu)}\nabla(T-T_0) = 0 \quad (1)$$

where G, ν, and α are the shear modulus, Poisson's ratio (drained), and the volumetric thermal expansion coefficient of the saturated porous medium, respectively; p is pressure, T is temperature; and the subscript zero indicates conditions at the initial state. Note that in its original version, BIOT2

Table 3. Constant Model Parameters

Parameter	Value	Unit	Reference
Thermal conductivity	2.8	W m^{-1} K^{-1}	*Turcotte and Schubert* [2002]
Rock density	2700	kg m^{-3}	*Turcotte and Schubert* [2002]
Source temperature	350	°C	
Thermal expansion coefficient	1×10^{-5}	$°C^{-1}$	*Wong and Brace* [1979] and *Bauer and Handin* [1983]
Poisson's ratio	0.25	dimensionless	*Christensen* [1996]

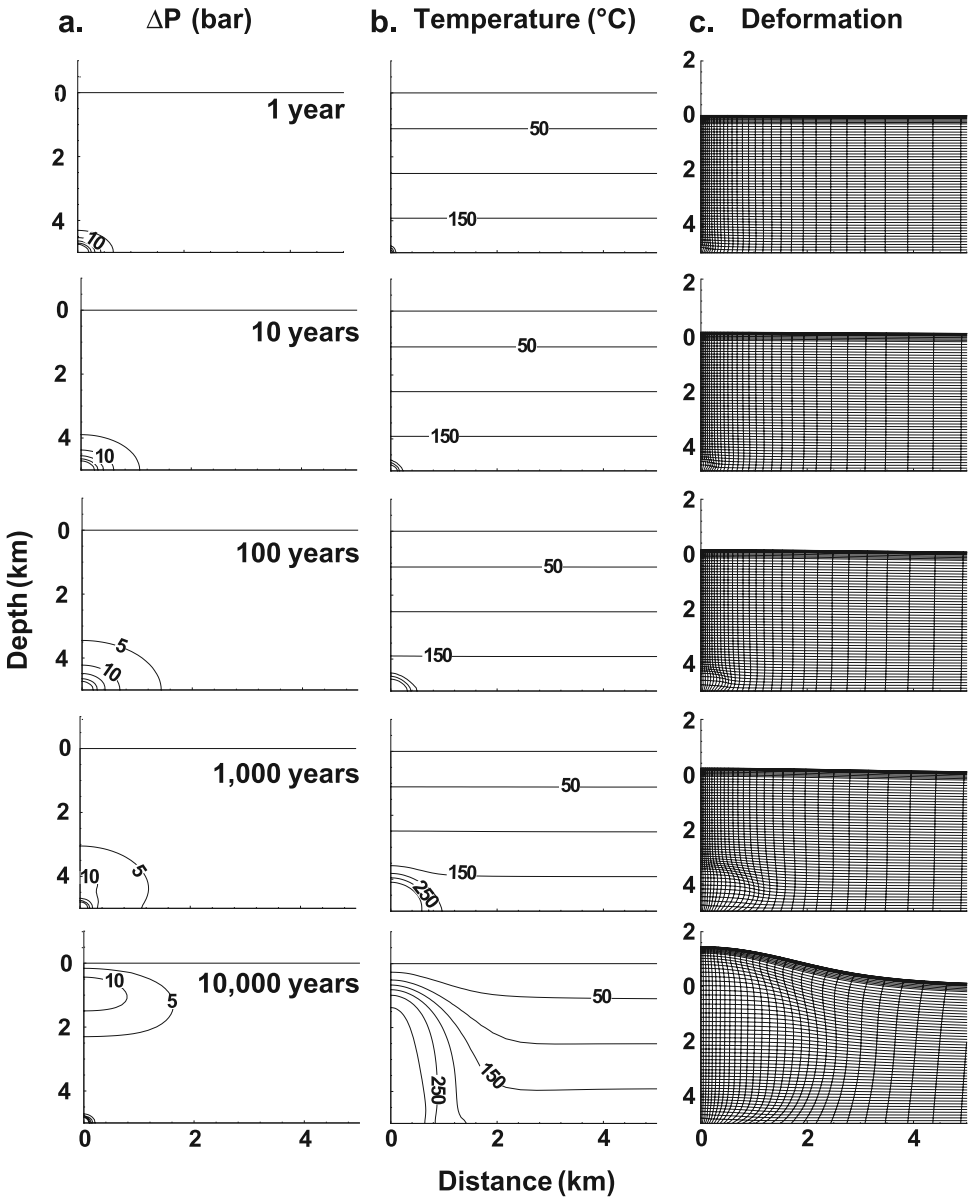

Figure 3. Time evolution in the reference simulation (Tables 2 and 3), showing (a) pressure change (ΔP) relative to pressure at the initial state, (b) temperature, and (c) deformation. For purpose of illustration, deformation is exaggerated 500 times, so that for example, a surface rise of 1 km corresponds to an actual rise of 2 m.

was designed for isothermal conditions, and therefore did not include the temperature term in equation (1). In other words, BIOT2 solves

$$G\nabla^2 \mathrm{u} + \frac{G}{1-2\nu}\nabla(\nabla \cdot \mathrm{u}) - \nabla(p - p_0) = 0 \qquad (2)$$

For the current application, temperature is introduced into BIOT2 by replacing $\nabla(p - p_0)$ in equation (2) with

$$\nabla\left[(p - p_0) + \frac{2G(1+\nu)\alpha}{3(1-2\nu)}(T - T_0)\right] \qquad (3)$$

Since both pressure and temperature are computed by TOUGH2, they are treated as specified values in BIOT2.

[12] Note that the gravity term does not appear in the deformation equation. This is because the deformation and stresses are referenced to an initial state that is in static equilibrium. Since the deformed state is also at static equilibrium, the gravity term drops out when then equation is formulated in terms of the change from the initial static state. In addition, BIOT2 implements an infinitesimal strain formulation in which the displacement is computed at each node (element corner); however, the computational mesh itself does not deform.

4. Model Assumptions and Simplifications

[13] The most significant simplification in this study is the emphasis on single phase (liquid), single component

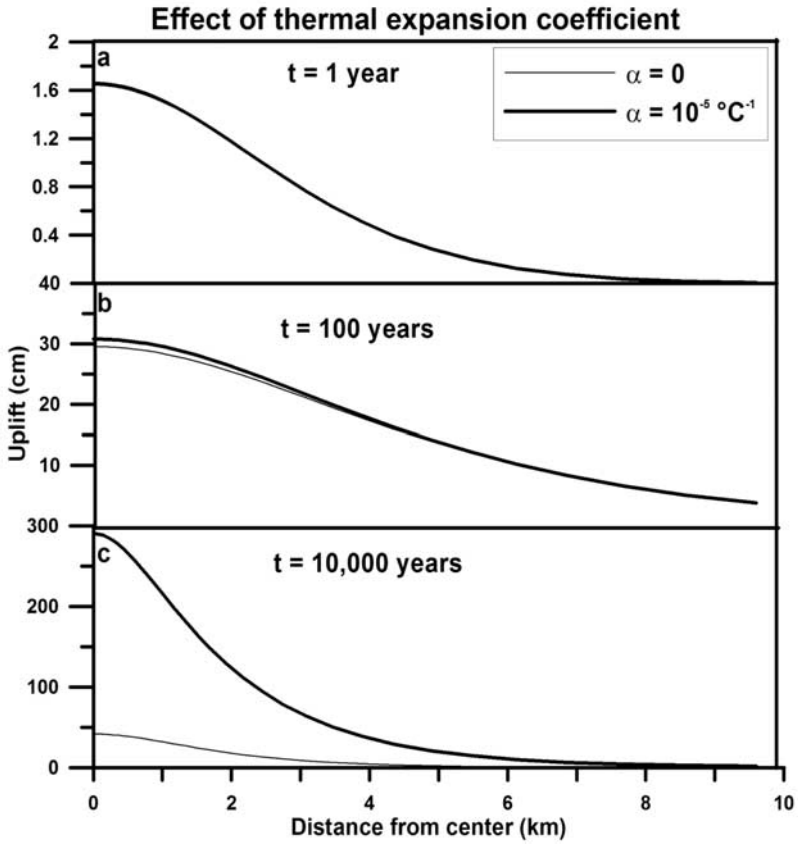

Figure 4. Effects of thermal expansion coefficient (a) after 1 simulation year, (b) 100 simulation years, and (c) 10,000 simulation years.

(pure water) fluid flow, except for a single simulation (CYCL-PERM; Table 2) where a steam phase develops (details in section 7.2). Many real caldera hydrothermal systems likely include vapor dominated, two-phase regions with large CO_2 fractions in the gas phase [*Chiodini et al.*, 2001, 2003; *Werner and Brantley*, 2003]. This single-phase simplification is not a requirement of the TOUGH2-BIOT2 model, but it allows us to more readily determine the sensitivity of key parameters and boundary conditions.

[14] In all but a small subset of the simulations we assume that model parameters remain constant throughout a 10,000 year simulation period. We further assume that all rock properties are homogeneous. In natural settings, the mechanical parameters are temperature and pressure dependent [*Heard and Page*, 1982], and permeability generally decreases with depth [*Manning and Ingebritsen*, 1999; *Saar and Manga*, 2004] and with time [*Hurwitz et al.*, 2002].

[15] We further assume that the water table coincides with the ground surface and that the topography is flat. In contrast to stratovolcanoes where topography is a major control on hydrodynamics [*Hurwitz et al.*, 2003], topographic gradients in calderas are in fact relatively small and the water table is usually close to the ground surface. Finally, we assume that the change in stress (as calculated by BIOT2) has no effect on permeability, porosity, or fluid flow. Such a one-way coupling approach (that is, from TOUGH2 to BIOT2 but not vice versa) has been also adopted in similar simulations [*Reid*, 2004; *Todesco et al.*, 2004].

5. Model Configuration and Boundary and Initial Conditions

[16] The model domain is a radially symmetric cylinder 3–8 km high with a radius of 50 km (Figure 2a). Simulations with a cylinder radius of 500 km produced identical results and demonstrated that there are no boundary effects. The model grid and results can be visualized on a rectangular cross section, with the left edge of the cross section coinciding with the central axis of the cylinder (Figure 2b). The cross section is divided into 50 columns and 56 layers. Horizontal grid spacing varies from 25 m at the center of the domain and increases toward the right-hand boundary. The vertical thickness of the uppermost layer is 1 m in order to represent the specified temperature and pressure at land surface in TOUGH2. Vertical resolution decreases downward, with 100 m thick layers throughout most of the domain (Figure 2b).

[17] The left-hand (center of the domain) and right-hand (outer edge of the domain) boundary conditions are set as insulating and impermeable in TOUGH2 (Figure 2b). The upper (land-surface) boundary is maintained at a constant temperature of 10°C and a pressure of 0.1 MPa to represent water table conditions. The basal boundary has a range of specified heat flux (100–250 mW/m^2), representing typical

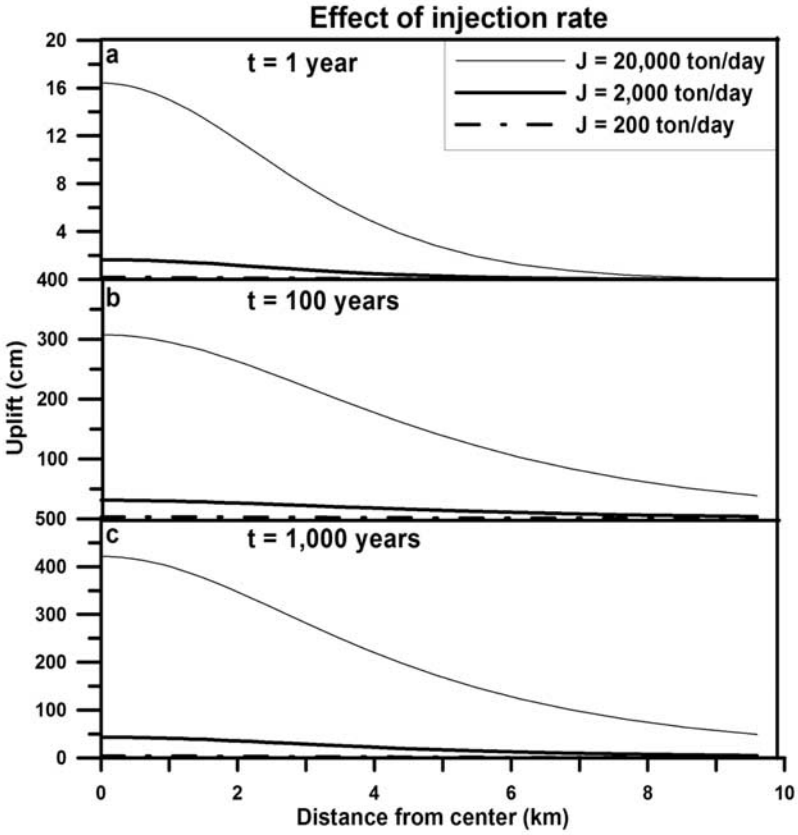

Figure 5. Effects of injection rate (series A in Table 2) on calculated ground surface displacement after (a) 1 simulation year, (b) 100 simulation years, and (c) 1000 simulation years.

background values for Quaternary calderas, and is impermeable except at the injection point located at the center of the bottom of the domain. Boundary conditions for BIOT2 include no displacement on the right-hand and bottom boundaries, vertical displacement only on the left boundary, and a traction-free surface on the upper boundary (Figure 2b).

[18] Initial conditions entail a hydrostatic pressure distribution throughout the domain and a linear temperature distribution between the fixed temperature upper boundary and the constant heat flux lower boundary. Numerical experiments were carried out for 10,000 simulation years to examine both short- and long-term deformation patterns. In most simulations parameters remain constant throughout the simulation; however, in two experiments the fluid injection rate or the permeability varied with time.

6. Key Parameters

[19] Because volcano hydrothermal systems are highly variable in space and time, the range of plausible values for most simulation parameters is large. Parameters that exhibit large variability in nature, or were regarded as highly uncertain, were the subject of our sensitivity analysis (Table 2). Those parameters which exhibit relatively small variability in natural systems were not varied (Table 3).

[20] The flux and composition of magmatic volatiles entering a caldera-hosted hydrothermal system are poorly constrained and depend in part on the depth, composition, and dimensions of the underlying magma body [*Podladchikov and Wickham*, 1994; *Hanson*, 1996]. In simulations of series A (Table 2) we invoke a magmatic fluid flux ranging from 200 to 20,000 t/d ($\sim$0.7 to 73 km^3 over the 10,000 simulated years) at the base of the domain. The higher value is equivalent to the flux liberated by the annual crystallization of 2×10^{-4} km^3 of granitic magma containing 5 wt % H_2O. These flux are generally larger than those modeled in previous studies [*Hanson*, 1996] but are consistent with the range of magmatic CO_2 fluxes measured in Long Valley (250 t/d) [*Gerlach et al.*, 1999], Campi Flegrei (1500 t/d) [*Chiodini et al.*, 2001], Taupo (1700 t/d) [*Seward and Kerrick*, 1996], and Yellowstone (45,000 t/d) [*Werner and Brantley*, 2003]. Magmatic H_2O fluxes are poorly constrained but are probably at least as large as CO_2 fluxes. For instance, in recent episodes of unrest in Campi Flegrei, H_2O flux was between 1500 and 3000 t/d, based on CO_2 flux measurements and molar H_2O/CO_2 determinations [*Chiodini et al.*, 2003].

[21] In simulations of series B the depth of the injection source was varied to represent varying depths to the brittle-ductile transition, which is traditionally estimated from the maximum depth of earthquakes within the caldera. The depths in several documented cases range from 3 to 8 km [*Waite and Smith*, 2002; *Hill et al.*, 2003].

[22] Permeabilities of igneous rocks are highly heterogeneous and range over at least 8 orders of magnitude at the scale of in situ hydraulic testing [*Brace*, 1984]. This range results largely from the variability of fracture density,

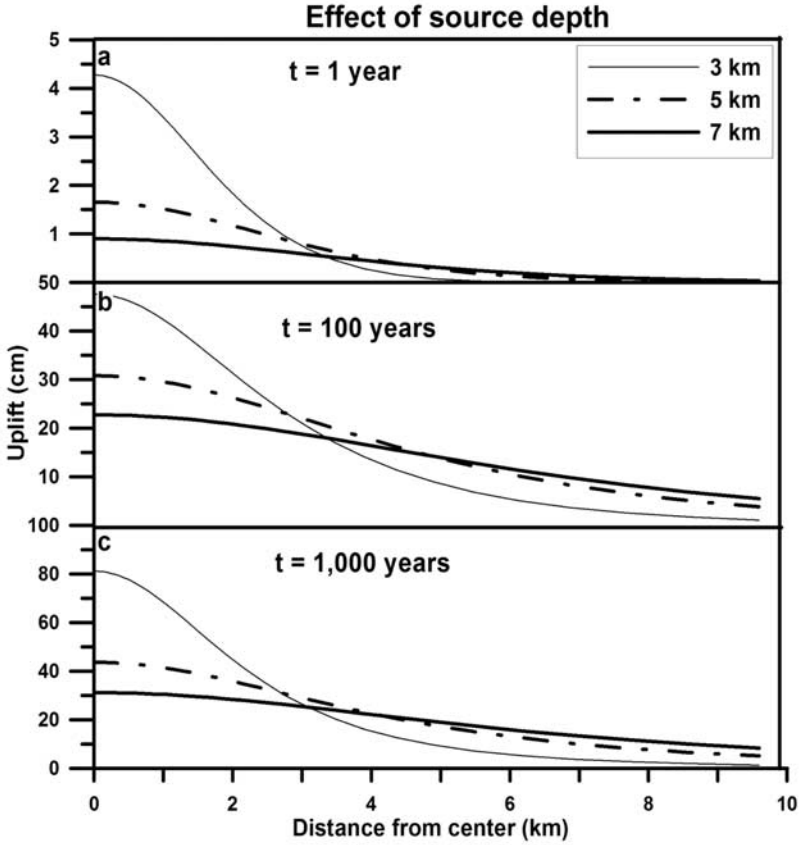

Figure 6. Effects of injection source depth (series B in Table 2) on calculated ground surface displacement after (a) 1 simulation year, (b) 100 simulation years, and (c) 1000 simulation years.

aperture, and geometry, and is also strongly influenced by the degree of hydrothermal alteration and fracture filling. The range of permeabilities we considered in simulations of series C in Table 2 (2×10^{-17} m^2 to 1×10^{-13} m^2) is limited by the large overpressures that form near the injection source at low permeabilities and numerical instabilities at high permeabilities. Fluid injection into low permeability rocks is likely to induce hydrofracturing, but such an effect was not incorporated into our model. The range of permeability values in our simulations is consistent with a large compilation of permeability measurements in geothermal fields [*Bjorbsson and Bodvarsson*, 1990].

[23] Direct measurements of permeability anisotropy are rare, and it is often neglected in numerical models. Calderas often consist of subparallel layered lava flows and pyroclastic units, suggesting that, on a large scale, permeability may be greater in the horizontal direction than in the vertical direction. Subvertical faults may act either as high-permeability conduits or as low-permeability seals that disrupt large-scale horizontal flow. In simulations of series D (Table 2), the general effects of anisotropic permeability are examined by varying the ratio of horizontal (k_x) to vertical (k_z) permeability.

[24] The value of thermal conductivity used in all simulations (Table 3) is an average for the continental crust. The range of heat flow values we invoke in simulations of series E (Table 2) is consistent with available data for Quaternary calderas [*Lachenbruch et al.*, 1976; *Bibby et al.*, 1995; *Wohletz et al.*, 1999].

[25] In linear elastic models, deformation of the crust scales inversely with shear (rigidity) modulus; as rigidity increases, less deformation occurs [*Turcotte and Schubert*, 2002]. Laboratory experiments at high pressures and temperatures indicate that the intrinsic shear modulus of crystalline rocks varies from 0.2 to 50 GPa, depending on rock type, temperature, pressure, and porosity [*Heard and Page*, 1982]. Large-scale crustal values, on the order of 30 GPa [*Turcotte and Schubert*, 2002], are commonly invoked for deformation models. However, several studies have suggested that the rigidity of warm volcanic rocks should be as low as 0.3 GPa [*Davis*, 1986]. In a majority of our simulations, the shear modulus was 1 GPa. However, in simulations of series F (Table 2), the effects of shear modulus values ranging between 1 and 30 GPa were examined.

[26] Typical values for the thermal expansion coefficient for saturated rocks at high temperature and pressure range from 5×10^{-6} °C^{-1} to 15×10^{-6} °C^{-1}, with a strong temperature dependence and a modest pressure dependence [*Wong and Brace*, 1979; *Heard and Page*, 1982; *Bauer and Handin*, 1983]. We invoke an average value of 10×10^{-6} °C^{-1} in all simulations (Table 3).

7. Simulation Results

[27] Following the onset of high-temperature fluid injection through the base of the model domain at $t = 0$, an overpressured zone with elevated temperature develops near

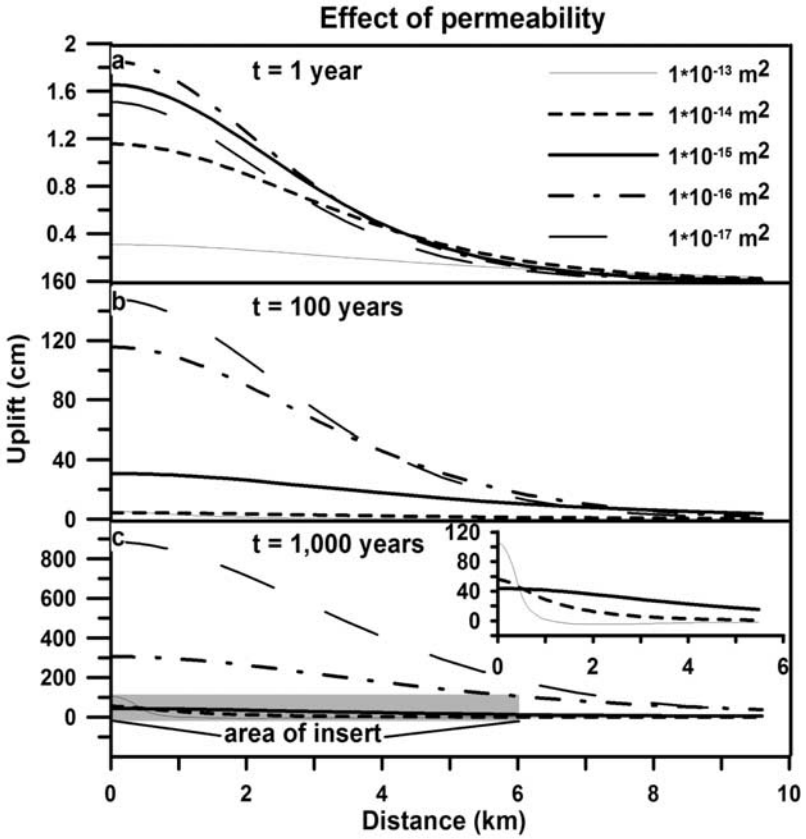

Figure 7. Effects of permeability (series C in Table 2) on calculated ground surface displacement after (a) 1 simulation year, (b) 100 simulation years, and (c) 1000 simulation years. Inset in Figure 7c shows in detail the displacement for simulations with higher permeability in the inner 5 km of the domain.

the injection point, causing local deformation (Figure 3). With time, the affected volume expands and at later times an additional overpressure zone develops at shallow depths (<2 km) and deformation is enhanced (Figure 3c).

[28] Both, poroelastic response to increased fluid pressure and thermoelastic rock expansion cause deformation. In order to isolate the effects of rock thermal expansion, the reference simulation (Tables 2 and 3) is compared with a simulation where the thermal expansion coefficient in BIOT2 is zero. There are no noticeable differences at early times (Figure 4a) and small differences after 100 simulation years (Figure 4b). However, after 10,000 simulation years, the GSD in the simulation including a nonzero thermal expansion coefficient is greater by a factor of 6 (Figure 4c) because upward migration of the thermal plume has caused the rock to expand and enhanced surface uplift.

7.1. Sensitivity Analysis

[29] To assess the sensitivity of the deformation field and GSD to key controlling parameters we examined the effect of a wide range of injection rates and depths, values of several rock properties, and the basal heat flux (Table 2).

[30] An order-of-magnitude increase in the injection rate (series A, Table 2) results in a fivefold increase in the GSD at the center of the domain after one simulation year (Figure 5a) and more than a factor of 10 after 1000 simulation years (Figure 5c). With higher injection rates the uplift is focused toward the center of the domain, whereas at lower injection rates uplift is more uniform.

[31] Testing the effect of source depth (series B, Table 2), showed that decreasing source depth increased calculated GSD (Figure 6). The difference in the calculated GSD between a source at 7 km and a source at 5 km is smaller than the calculated GSD between a source at 5 km and a source at 3 km. Some of this difference is due to the increasing effect of rock thermal expansion as the injection source is shallower. Decreasing the depth of the injection source also results in a more focused deformation field in the center of the domain.

[32] Varying permeability over almost 5 orders of magnitude (series C, Table 2) yielded a complex pattern of response (Figure 7). After 1 simulation year, uplift in the simulation with the lowest permeability (2×10^{-17} m^2) is less than the uplift with higher permeabilities of 1×10^{-15} m^2 and 1×10^{-16} m^2 (Figure 7a). However, at later times, uplift is larger when permeabilities are lower (Figures 7b and 7c). For permeabilities $\geq 1 \times 10^{-14}$ m^2, uplift rates are relatively small and focused near the center of the domain (Figure 7c, inset). At later times, uplift in the center of the domain, in the simulation with a permeability of 1×10^{-13} m^2 is greater than the uplift associated with the simulation with a permeability of 1×10^{-14} m^2 (inset in Figure 7c). This phenomenon results from the enhanced upward flow of the hot fluid at higher permeabilities, which causes an increase in rock thermal expansion at shallow depths.

[33] To assess the effects of permeability anisotropy, we fixed the horizontal permeability at 1×10^{-15} m^2 and decreased the vertical permeability by 1 and 2 orders of

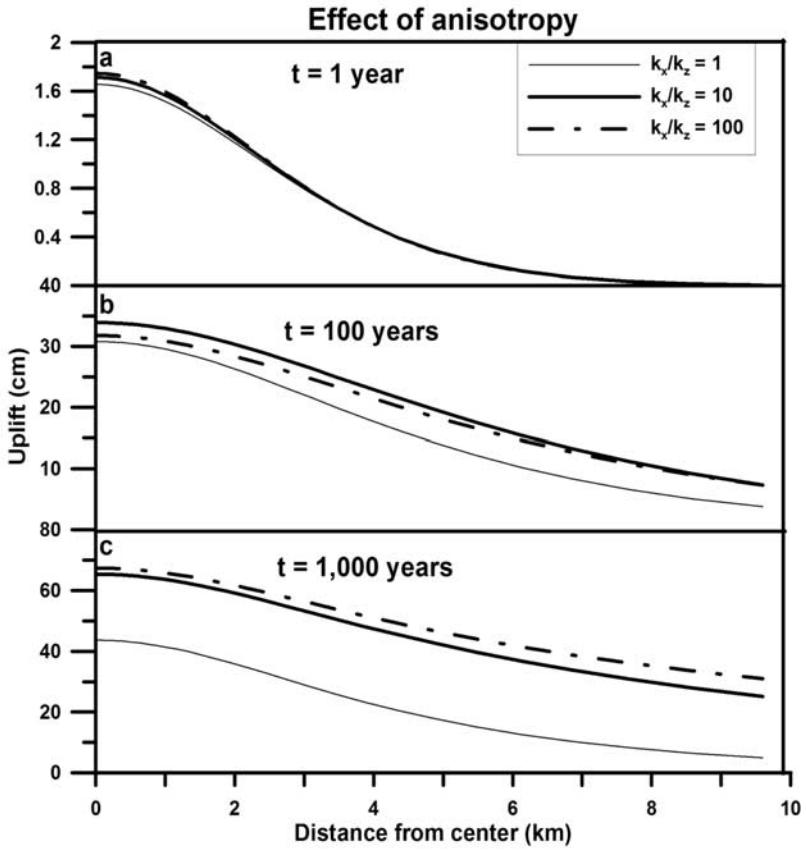

Figure 8. Effects of permeability anisotropy (series D in Table 2) on calculated ground surface displacement after (a) 1 simulation year, (b) 100 simulation years, and (c) 1000 simulation years.

magnitude (series D, Table 2). The increase in anisotropy had a minor effect after one and ten years (Figures 8a and 8b), but the effect is significant after 1000 simulation years (Figure 8c). Lateral flow of the high-temperature fluid is enhanced as the anisotropy increases, reducing heating and rock thermal expansion near the center of the domain.

[34] Increasing the basal heat flux to 200 mW/m^2 (series E, Table 2) slightly decreases GSD rates (Figure 9). The higher temperatures at the bottom of the domain reduce water viscosity which, in turn, leads to lower pore fluid pressures and reduced deformation. The magnitude of the effect is limited by the fact that the thermal state is dominated by the high-temperature (350°C) fluids at the center of the domain.

[35] The rigidity of the domain has a substantial effect on GSD. Increased displacements do not scale linearly with increased shear modulus (Figure 10). For example, a 30-fold increase of the shear modulus (series F, Table 2) results in a fivefold increase in GSD at the center of the domain after one simulation year (Figure 10a) and a 3.5-fold increase after 1000 simulation years (Figure 10c). Porosity changes within the range tested (series G in Table 2) have minor effects on the calculated displacements.

7.2. Subsidence

[36] One of the limitations of classic elastic models for caldera deformation is the lack of a straightforward explanation for subsidence. In simulations of series H (Table 2), we applied two different poroelastic subsidence scenarios based on the conceptual model presented in section 2, using parameters of the reference simulation (Tables 2 and 3). In the first simulation, the injection source varied episodically to represent episodic magma degassing (simulation CYCL-INJ in Table 2). Thirty-year on-off cycles (arbitrary value) were continued for a total of 600 simulation years. When injection ceased, subsidence began instantaneously and continued gradually over the following 30 years. Upon renewed injection, gradual uplift occurred for the next 30 years (Figure 11a).

[37] In the second simulation, permeability was varied cyclically from 1×10^{-15} m^2 to 1×10^{-14} m^2, to represent hydrofracturing and sealing (simulation CYCL-PERM in Table 2), with 30-year cycles of low and high permeability continued for 600 simulation years (Figure 11b). When permeability was increased, subsidence also commenced instantaneously, but in contrast to the variable source scenario, the return to near-initial elevation (at t = 0) was very rapid (within 1 year, Figure 11b). In the cyclic permeability experiment net uplift accelerated after about 220 simulation years. The accelerated uplift occurred as a vapor phase formed accelerating the ascent of the low-density thermal plume to shallow depths where thermal expansion became significant.

7.3. Comparison With Measured Deformation in Calderas

[38] We carried out a few additional simulations intended to mimic the major characteristics of observed

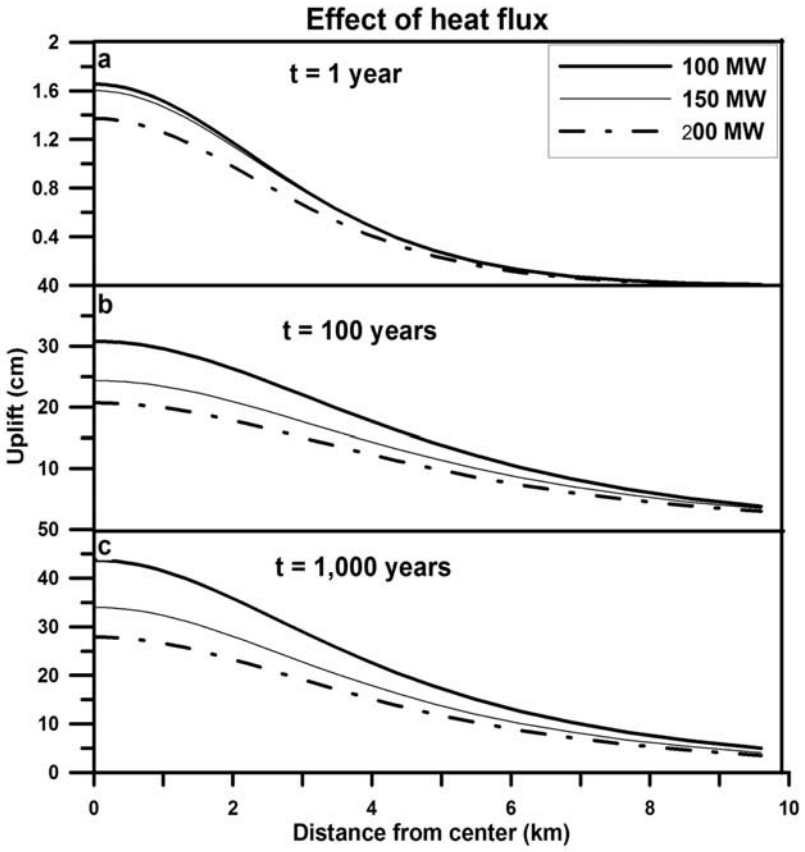

Figure 9. Effects of basal heat flux (series E in Table 2) on calculated ground surface displacement after (a) 1 simulation year, (b) 100 simulation years, and (c) 1000 simulation years.

GSD in selected calderas (series I in Table 2). The GSD data from Campi Flegrei for the period between January 1981 and September 1983 has been modeled by volume increase of a penny-shaped crack filled with a low-density fluid (600 kg/m^3) and embedded in an elastic half-space at a depth of 2.6 km (Figure 12a) [*Battaglia et al.*, 2006]. The same data were successfully simulated with experiment CF-3 km (Table 2) with an injection source at 3 km (Figure 11a) and assuming that t = 0 and the onset of fluid injection occurred in January 1981 and continued until September 1983. Deeper injection sources in the model domain were not capable of inducing such high simulated uplift rates.

[39] Inversion of geodetic data from Long Valley caldera for the period between 1982 and 1999 was previously modeled by volume change of a vertical prolate ellipsoidal source at a depth of ~6 km in an elastic half-space (Figure 12b) [*Battaglia et al.*, 2003]. A good fit for GSD data from Long Valley for the period from 1995 to 2000 was also attained using a dipping prolate ellipsoidal source at ~6 km in a viscoelastic half-space [*Newman et al.*, 2006]. Interpretation of microgravity data is apparently more compatible with the addition of silicic magma into the ellipsoidal than a hydrothermal source [*Battaglia et al.*, 2003]. Nevertheless, several studies have suggested that much of the unrest in Long Valley is in fact driven by aqueous fluids and/or gas [*Foulger et al.*, 2003; *Hill et al.*, 2003; *Roeloffs et al.*, 2003]. Simulation of the GSD in Long Valley using an injection source at 5 km (LVC-5 km in Table 2) captured the magnitude and rate of uplift in the center of the domain, but could not reproduce the radial extent of the observed uplift (Figure 12b). Increasing the depth of the source to 8 km (LVC-8 km in Table 2) generates a wider area of deformation, but still narrower than the observations (Figure 12b). This mismatch implies that if injection of hydrothermal fluids actually did induce surface uplift during the period of unrest in the 1980s and 1990s in Long Valley, either there were additional fluid sources at greater radial distances from the center of inflation, or the single injection source had a larger radius. These same constraints on the effectiveness of fluid injection also likely apply to other large calderas such as Yellowstone and Taupo (Table 1) where the radius of deformation is large.

8. Discussion

[40] Relatively small changes in the values of the key controlling parameters can lead to large differences in the rate, magnitude, and geometry of GSD (Figures 4–11). Under a wide and plausible range of parameter values, rock deformation induced by pore pressure transients at various timescales may provide a feasible explanation for GSD in calderas. However, the results are nonunique in the sense that many combinations of parameters can result in a very

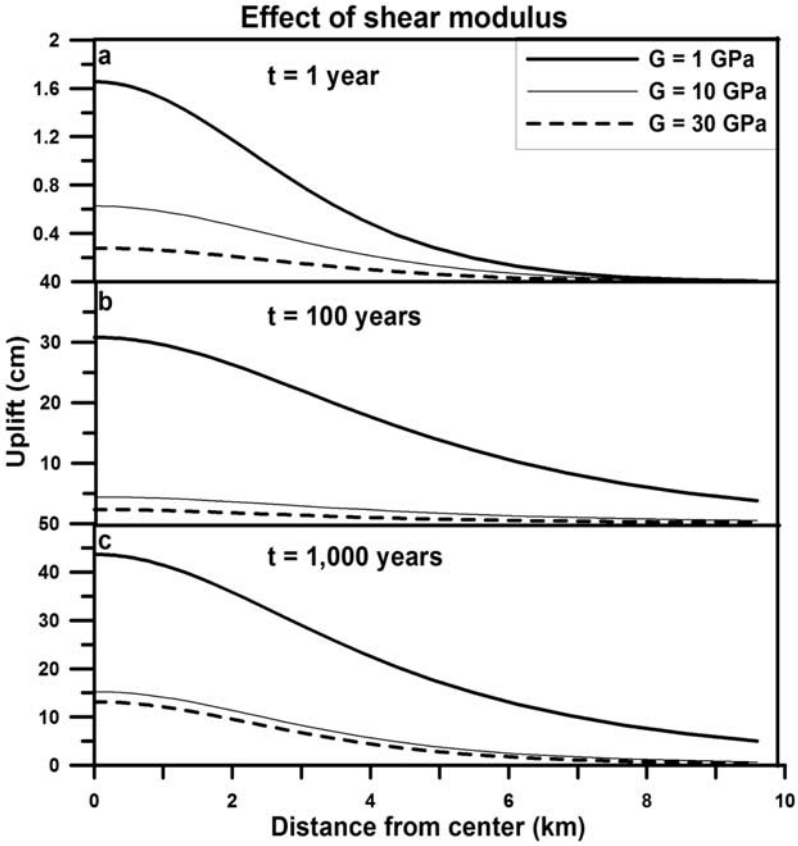

Figure 10. Effects of shear modulus (series F in Table 2) on calculated ground surface displacement after (a) 1 simulation year, (b) 100 simulation years, and (c) 1000 simulation years.

similar deformation field. Higher injection rates (Figure 5), shallower injection sources (Figure 6), lower permeabilities (Figure 7), higher permeability anisotropy (Figure 8), lower basal heat flux (Figure 9), and lower shear modulus (Figure 10), generally lead to greater deformation and GSD.

[41] At annual to decadal timescales, fluid volume increase is the dominant process inducing deformation, whereas over longer times (centennial and millennial) when hydrothermal upflow has heated larger volumes of crust, rock thermal expansion becomes more significant. Thus, at some calderas, measured displacement fields could represent a delayed response to magma degassing events that commenced long ago.

[42] In absence of independent data, it is difficult to determine whether GSD in calderas is induced by injection of hydrothermal fluids into the shallow crust or by magma intrusion. Several lines of indirect evidence suggest that in some cases subsurface volume changes and caldera deformation may be associated with the dynamics of a low-viscosity, low-density, gas-rich fluid at shallow depths. For example, the occurrence of numerous Holocene hydrothermal explosion craters in Yellowstone [*Muffler et al.*, 1971] have been associated with episodes of Yellowstone Caldera uplift [*Pierce et al.*, 2002], indicating that large water and/or gas pressures are intermittently attained in the shallow subsurface. In Campi Flegrei, caldera inflation-deflation cycles correlate with CO_2/H_2O transients in vents, suggesting that CO_2 pressures are high during inflation periods [*Chiodini et al.*, 2003]. The 45 ± 16 kt/d of diffuse magmatic CO_2 flux emitted from the Yellowstone volcanic system [*Werner and Brantley*, 2003] cannot be sustained by discrete episodes of basalt intrusion into the upper crust (<0.03 km^3/yr) during periods of inflation [*Dzurisin et al.*, 1994; *Wicks et al.*, 1998], suggesting that perhaps also in Yellowstone some of the deformation is associated with the dynamics of CO_2 in the hydrothermal system. The involvement of gas-rich fluids in the deformation of the Yellowstone caldera may be inferred by the abrupt change from uplift to subsidence in 1985 and from subsidence to uplift in 1995, which in each instance were followed by large earthquake swarms migrating away from the caldera at rapid rates [*Waite and Smith*, 2002].

[43] Recent developments in satellite-based geodetic techniques will likely enable better spatial and temporal resolution of GSD in calderas and thus potentially provide better constraints on subsurface fluid dynamics. Continuous, high-precision microgravity measurements may discriminate between magma intrusion and hydrothermal injection at shallow depths, because the density of magma differs by a factor of 3 or more from the density of superheated vapor or gas [*Rymer*, 1994; *Gottsmann and Rymer*, 2002; *de Zeeuw-van Dalfsen et al.*, 2005]. Combining such geodetic and microgravity data with quantitative dynamic models should provide insight into the nature of the fluid inducing deformation.

[44] A more direct way to detect water pressure transients in the shallow subsurface of calderas is through continuous and precise pressure measurements in deep drillholes.

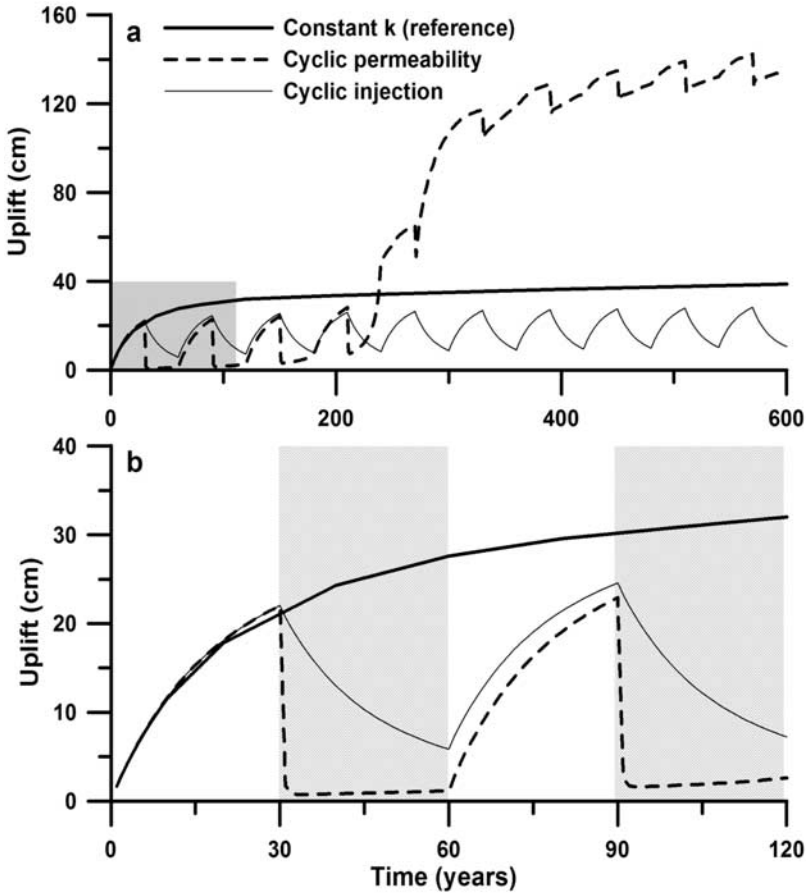

Figure 11. Effects of cyclic variations in permeability and injection rate on calculated GSD and inflation-deflation cycles (a) results from 600 simulation years. (b) Shaded area in Figure 11a shown in greater detail. Shaded areas represent periods of no injection or increased permeability.

However, in many calderas there are no deep wells and in others, such as Taupo and Long Valley, geothermal production introduces large human-induced noise into the data.

[45] For the sake of simplicity, this study focused on simulations of poroelastic deformation induced by liquid groundwater flow. Future studies will consider the effects of multiphase and multicomponent H_2O-CO_2-NaCl subsurface fluid flow. The assumption of "one-way coupling" in this study does limit the general applicability of the simulation results. To implement a fully coupled simulation, it is necessary to consider the interaction between stress change, pressure, and permeability. We partially examined the effect of stress change on pressure (assuming permeability is not affected) by solving the fully coupled Biot equations under single phase, saturated isothermal conditions. For the fluid injection scenarios considered in this paper, we found that the one-way coupling simulation differed from the fully coupled simulation by less than 10%. By contrast, the effects of permeability change can be drastic. Our simulation of cyclically varying permeability (CYCL-PERM) is a crude attempt to illustrate the effects of permeability change without explicitly coupling the permeability change to pressure change. This type of coupling deserves a more rigorous treatment in future studies.

[46] The feasibility of large GSD resulting from aqueous fluid overpressure, as demonstrated in this study, suggests that such phenomena should be considered in hazard assessments of active calderas. The consequences resulting from large groundwater overpressures may be very different from those of magma ascent into the shallow crust. For example, large aqueous overpressures might result in hydrothermal explosions, whereas magma ascent into the shallow crust might signal an impeding volcanic eruption.

9. Conclusions

[47] We conducted numerical simulations of hydrothermal fluid flow and associated ground surface displacement (GSD) in calderas. Simulation results reveal the following:

[48] 1. Small changes in the values of key controlling parameters, particularly permeability and its anisotropy, the injection rate and depth, and the shear modulus may lead to large differences in the rate, magnitude, and geometry of GSD.

[49] 2. Subsidence was simulated successfully both by terminating the injection of hot fluid into the model domain and by increasing the permeability after uplift occurred. Subsidence was more abrupt in the case of a permeability increase.

[50] 3. The major patterns of ground surface uplift in Campi Flegrei were effectively mimicked by the simula-

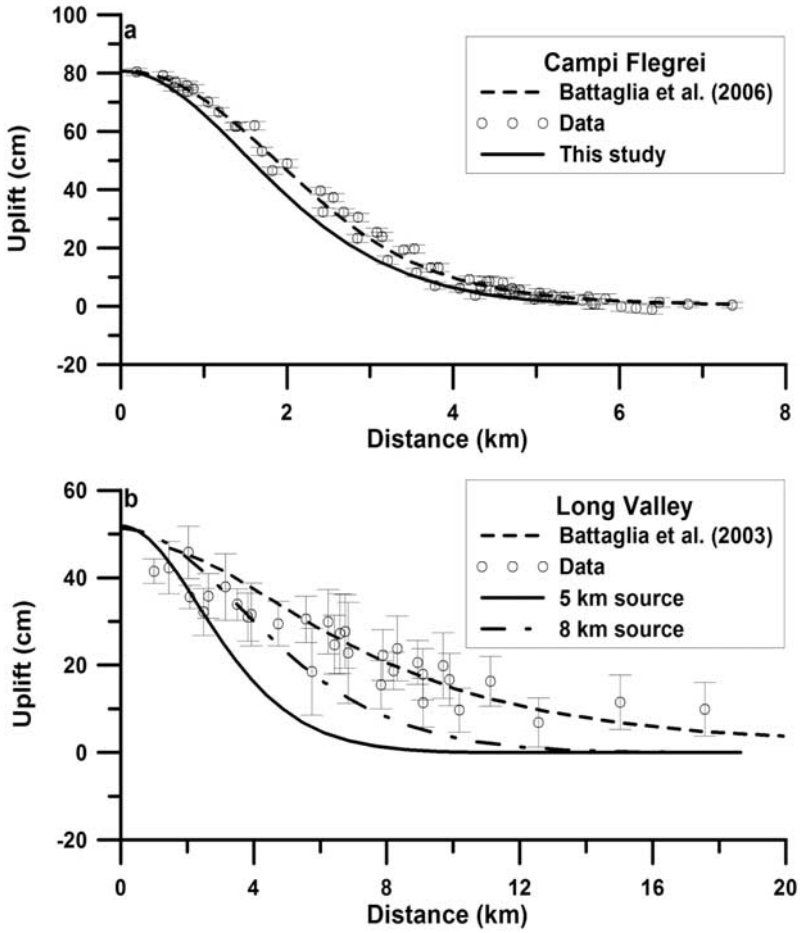

Figure 12. (a) Observed Campi Flegrei vertical ground surface displacements (circles) with two standard deviation error bars, calculated displacements from an elastic half-space model (dashed line) [*Battaglia et al.*, 2006], and results of simulation CF-3 km (2.5 simulation years) from this study (solid curve) and (b) observed Long Valley GSD (circles) with two standard deviation error bars, calculated displacements from an elastic half-space model (dashed line) [*Battaglia et al.*, 2003], and results of simulation LVC-5 km (solid curve) and LVC-8 km (dash-dotted curve), simulating 17 years of deformation. Simulation parameters are listed in Table 2.

tions, but only some of uplift characteristics in Long Valley were reproduced.

[51] 4. On the basis of the numerical experiments, and a growing number of observations which indicate a causal link between GSD and dynamics of hydrothermal fluids and/or gases, we propose that future studies should focus on resolving the nature of the fluid causing GSD (e.g., magma or aqueous fluid and gas).

[52] **Acknowledgments.** Funding for this research came from the U.S. Geological Survey Volcano Hazards Program. L. B. Christiansen was funded by an associateship from the National Research Council. We thank Maurizio Battaglia for providing the Long Valley and Campi Flegrei data and simulation results. Sebastian Geiger, Mark Reid, Martin Saar, Ward Sanford and Wayne Thatcher are thanked for constructive reviews.

References

Archbold, M. J., C. O. McKee, B. Talai, J. Mori, and P. de Saint Ours (1988), Electronic distance measuring network monitoring during the Rabaul seismicity-deformational crisis of 1983–1985, *J. Geophys. Res.*, *93*, 12,123–12,136.

Battaglia, M., P. Segall, and C. Roberts (2003), The mechanics of unrest at Long Valley caldera, California: 2. Constraining the nature of the source using geodetic and micro-gravity data, *J. Volcanol. Geotherm. Res.*, *127*, 219–245.

Battaglia, M., C. Troise, F. Obrizzo, F. Pingue, and G. De Natale (2006), Evidence for fluid migration as the source of deformation at Campi Flegrei caldera (Italy), *Geophys. Res. Lett.*, *33*, L01307, doi:10.1029/2005GL024904.

Bauer, S. J., and J. Handin (1983), Thermal expansion and cracking of three confined, water-saturated igneous rocks to 800°C, *Rock Mech. Rock Eng.*, *16*, 181–198.

Beauducel, F., G. De Natale, F. Obrizzo, and F. Pingue (2004), 3-D modelling of Campi Flegrei ground deformations: Role of caldera boundary discontinuities, *Pure Appl. Geophys.*, *161*, 1329–1344.

Bibby, H. M., T. G. Caldwell, F. J. Davey, and T. H. Webb (1995), Geophysical evidence on the structure of the Taupo Volcanic Zone and its hydrothermal circulation, *J. Volcanol. Geotherm. Res.*, *68*, 29–58.

Bjorbsson, G., and G. Bodvarsson (1990), A survey of geothermal reservoir properties, *Geothermics*, *19*, 17–27.

Bonafede, M. (1991), Hot fluid migration: An efficient source of ground deformation: Application to the 1982–1985 crisis at Campi Flegrei, Italy, *J. Volcanol. Geotherm. Res.*, *48*, 187–198.

Bonafede, M., M. Dragoni, and F. Quareni (1986), Displacement and stress fields produced by a centre of dilation and by a pressure source in a viscoelastic half-space: Application to the study of ground deformation and seismic activity at Campi Flegrei, Italy, *Geophys. J. R. Astron. Soc.*, *87*, 455–485.

Brace, W. F. (1984), Permeability of crystalline rocks: New in situ measurements, *J. Geophys. Res.*, *89*, 4327–4330.

Chiodini, G., F. Frondini, C. Cardellini, D. Granieri, L. Marini, and G. Ventura (2001), CO_2 degassing and energy release at Solfatara volcano, Campi Flegrei, Italy, *J. Geophys. Res.*, *106*, 16,213–16,221.

Chiodini, G., M. Todesco, S. Caliro, C. Del Gaudio, G. Macedonio, and M. Russo (2003), Magma degassing as a trigger of bradyseismic events: The case of Phlegrean Fields (Italy), *Geophys. Res. Lett.*, *30*(8), 1434, doi:10.1029/2002GL016790.

Christensen, N. I. (1996), Poisson's ratio and crustal seismology, *J. Geophys. Res.*, *101*, 3139–3156.

Davis, P. M. (1986), Surface deformation due to inflation of an arbitrarily oriented triaxial ellipsoidal cavity in an elastic half-space, with reference to Kilauea Volcano, Hawaii, *J. Geophys. Res.*, *91*, 7429–7438.

De Natale, G., C. Troise, and F. Pingue (2001), A mechanical fluid-dynamical model for ground movements at Campi Flegrei caldera, *J. Geodyn.*, *32*, 487–517.

de Zeeuw-van Dalfsen, E., H. Rymer, F. Sigmundsson, and E. Sturkell (2005), Net gravity decrease at Askja volcano, Iceland: Constraints on processes responsible for continuous caldera deflation, 1988–2003, *J. Volcanol. Geotherm. Res.*, *139*, 227–239.

Dvorak, J. J., and D. Dzurisin (1997), Volcano geodesy: The search for magma reservoirs and the formation of eruptive vents, *Rev. Geophys.*, *35*, 343–384.

Dzurisin, D. (2003), A comprehensive approach to monitoring volcano deformation as a window on the eruption cycle, *Rev. Geophys.*, *41*(1), 1001, doi:10.1029/2001RG000107.

Dzurisin, D., J. C. Savage, and R. O. Fournier (1990), Recent crustal subsidence at Yellowstone Caldera, Wyoming, *Bull. Volcanol.*, *52*, 247–270.

Dzurisin, D., K. M. Yamashita, and J. W. Kleinman (1994), Mechanisms of crustal uplift and subsidence at the Yellowstone Caldera, Wyoming, *Bull. Volcanol.*, *56*, 261–270.

Dzurisin, D., C. Wicks, and W. Thatcher (1999), Renewed uplift at the Yellowstone Caldera measured by leveling surveys and satellite radar interferometry, *Bull. Volcanol.*, *61*, 349–355.

Fialko, Y., Y. Khazan, and M. Simons (2001), Deformation due to a pressurized horizontal circular crack in an elastic half-space, with applications to volcano geodesy, *Geophys. J. Int.*, *146*, 181–190.

Foulger, G. R., B. R. Julian, A. M. Pitt, D. P. Hill, P. E. Malin, and E. Shalev (2003), Three-dimensional crustal structure of Long Valley caldera, California, and evidence for the migration of CO_2 under Mammoth Mountain, *J. Geophys. Res.*, *108*(B3), 2147, doi:10.1029/2000JB000041.

Fournier, R. O. (1999), Hydrothermal processes related to movement of fluid from plastic into brittle rock in the magmatic-epithermal environment, *Econ. Geol.*, *94*, 1193–1211.

Gerlach, T. M., M. P. Doukas, K. A. McGee, and R. Kessler (1999), Airborne detection of diffuse carbon dioxide emissions at Mammoth Mountain, California, *Geophys. Res. Lett.*, *26*, 3661–3664.

Gottsmann, J., and H. Rymer (2002), Deflation during caldera unrest: Constraints on subsurface processes and hazard prediction from gravity-height data, *Bull. Volcanol.*, *64*, 338–348.

Hanson, R. B. (1996), Hydrodynamics of magmatic and meteoric fluids in the vicinity of granitic intrusions, *Spec. Pap. Geol. Soc. Am.*, *315*, 251–259.

Heard, H. C., and L. Page (1982), Elastic moduli, thermal expansion, and inferred permeability of two granites to 350°C and 55 megapascals, *J. Geophys. Res.*, *87*, 9340–9348.

Hill, D. P., J. O. Langbein, and S. Prejean (2003), Relations between seismicity and deformation during unrest in Long Valley Caldera, California, from 1995 through 1999, *J. Volcanol. Geotherm. Res.*, *127*, 175–193.

Hsieh, P. A. (1996), Deformation-induced changes in hydraulic head during ground-water withdrawal, *Ground Water*, *34*, 1082–1089.

Hurwitz, S., S. E. Ingebritsen, and M. L. Sorey (2002), Episodic thermal perturbations associated with groundwater flow: An example from Kilauea Volcano, Hawaii, *J. Geophys. Res.*, *107*(B11), 2297, doi:10.1029/2001JB001654.

Hurwitz, S., K. L. Kipp, S. E. Ingebritsen, and M. E. Reid (2003), Groundwater flow, heat transport, and water table position within volcanic edifices: Implications for volcanic processes in the Cascade Range, *J. Geophys. Res.*, *108*(B12), 2557, doi:10.1029/2003JB002565.

Kwoun, O. I., Z. Lu, C. Neal, and C. Wicks Jr. (2006), Quiescent deformation of the Aniakchak Caldera, Alaska mapped by InSAR, *Geology*, *34*, 5–8.

Lachenbruch, A. H., J. H. Sass, R. J. Munroe, and T. H. Moses Jr. (1976), Geothermal setting and simple heat conduction models for the Long Valley Caldera, *J. Geophys. Res.*, *81*, 769–784.

Langbein, J. O. (2003), Deformation of the Long Valley Caldera, California: Inferences from measurements from 1988 to 2001, *J. Volcanol. Geotherm. Res.*, *127*, 247–267.

Lipman, P. W. (1984), The roots of ash flow calderas in western North America: Windows into the tops of granitic batholiths, *J. Geophys. Res.*, *89*, 8801–8841.

Lipman, P. W. (1997), Subsidence of ash-flow calderas: Relation to caldera size and magma-chamber geometry, *Bull. Volcanol.*, *59*, 198–218.

Lipman, P. W. (2000), Calderas, in *Encyclopedia of Volcanoes*, edited by H. Sigurdsson et al., pp. 643–662, Elsevier, New York.

Manning, C. E., and S. E. Ingebritsen (1999), Permeability of the continental crust: Implications of geothermal data and metamorphic systems, *Rev. Geophys.*, *37*, 127–150.

McKee, C. O., P. L. Lowenstein, P. D. S. Ours, B. Talai, I. Itikarai, and J. J. Mori (1984), Seismic and ground deformation crisis at Rabaul Caldera: Prelude to an eruption?, *Bull. Volcanol.*, *47*, 397–411.

Mogi, K. (1958), Relations of the eruptions of various volcanoes and the deformation of ground surfaces around them, *Bull. Earthquake Res. Inst. Tokyo Univ.*, *36*, 94–134.

Morhange, C., N. Marriner, J. Laborel, M. Todesco, and C. Oberlin (2006), Rapid sea-level movements and noneruptive crustal deformations in the Phlegrean Fields caldera, Italy, *Geology*, *34*, 93–96.

Muffler, L. J. P., D. E. White, and A. H. Truesdell (1971), Hydrothermal explosion craters in Yellowstone National Park, *Geol. Soc. Am. Bull.*, *82*, 723–740.

Newhall, C. G., and D. Dzurisin (1988), Historical unrest at large calderas of the world, *U.S. Geol. Surv. Bull.*, *1855*, 1108 pp.

Newhall, C. G., H. Cheng, and R. L. Edwards (1998), New estimates of uplift rates of Iwo-Jima, Japan, *Eos Trans. AGU*, *79*(45), Fall Meet. Suppl., F950.

Newman, A. V., T. H. Dixon, G. I. Ofoegbu, and J. E. Dixon (2001), Geodetic and seismic constraints on recent activity at Long Valley Caldera, California: Evidence for viscoelastic rheology, *J. Volcanol. Geotherm. Res.*, *105*, 183–206.

Newman, A. V., T. H. Dixon, and N. Gourmelen (2006), A four-dimensional viscoelastic deformation model for Long Valley Caldera, California, between 1995 and 2000, *J. Volcanol. Geotherm. Res.*, *150*, 244–269.

Orsi, G., L. Civetta, C. Del Gaudio, S. De Vita, M. A. Di Vito, R. Isaia, S. M. Petrazzuoli, G. P. Ricciardi, and C. Ricco (1999), Short-term ground deformations and seismicity in the resurgent Campi Flegrei caldera (Italy): An example of active block-resurgence in a densely populated area, *J. Volcanol. Geotherm. Res.*, *91*, 415–451.

Otway, P. M., G. H. Blick, and B. J. Scott (2002), Vertical deformation at Lake Taupo, New Zealand, from lake levelling surveys, 1979–99, *N. Z. J. Geol. Geophys.*, *45*, 121–132.

Pelton, J. R., and R. B. Smith (1979), Recent crustal uplift in Yellowstone National Park, *Science*, *206*, 1179–1182.

Pierce, K. L., K. P. Cannon, G. A. Meyer, M. J. Trebesch, and R. Watts (2002), Post-glacial inflation-deflation cycles, tilting, and faulting in the Yellowstone Caldera based on Yellowstone lake shorelines, *U.S. Geol. Surv. Open File Rep., 02-0142*, 62 pp.

Podladchikov, Y. Y., and S. M. Wickham (1994), Crystallization of hydrous magmas: Calculation of associated thermal effects, volatile fluxes, and isotopic alteration, *J. Geol.*, *102*, 25–45.

Poland, M., M. Hamburger, and A. Newman (2006), The changing shapes of active volcanoes: History, evolution, and future challenges for volcano geodesy, *J. Volcanol. Geotherm. Res.*, *150*, 1–13.

Pritchard, M. E., and M. Simons (2002), A satellite geodetic survey of large-scale deformation of volcanic centres in the central Andes, *Nature*, *418*, 167–171.

Pruess, K., C. Oldenburg, and G. Moridis (1999), TOUGH2 user's guide, version 2.0, *Paper LBNL-43134*, Lawrence Berkeley Natl. Lab., Berkeley, Calif.

Reid, M. E. (2004), Massive collapse of volcano edifices triggered by hydrothermal pressurization, *Geology*, *32*, 373–376.

Roeloffs, E., M. Sneed, D. L. Galloway, M. L. Sorey, C. D. Farrar, J. F. Howle, and J. Huges (2003), Water-level changes induced by local and distant earthquakes at Long Valley caldera, California, *J. Volcanol. Geotherm. Res.*, *127*, 269–303.

Rymer, H. (1994), Microgravity change as a precursor to volcanic activity, *J. Volcanol. Geotherm. Res.*, *61*, 311–328.

Saar, M. O., and M. Manga (2004), Depth dependence of permeability in the Oregon Cascades inferred from hydrogeologic, thermal, seismic, and magmatic modeling constraints, *J. Geophys. Res.*, *109*, B04204, doi:10.1029/2003JB002855.

Seward, T. M., and D. M. Kerrick (1996), Hydrothermal CO_2 emission from the Taupo Volcanic Zone, New Zealand, *Earth Planet. Sci. Lett.*, *139*, 105–113.

Todesco, M., J. Rutqvist, G. Chiodini, K. Pruess, and C. M. Oldenburg (2004), Modeling of recent volcanic episodes at Phlegrean Fields (Italy): Geochemical variations and ground deformation, *Geothermics*, *33*, 531–547.

Turcotte, D. L., and G. Schubert (2002), *Geodynamics*, 2nd ed., 472 pp., Cambridge Univ. Press, New York.

Ukawa, M., E. Fujita, H. Ueda, T. Kumagai, H. Nakajima, and H. Morita (2006), Long-term geodetic measurements of large scale deformation at Iwo-jima caldera, Japan, *J. Volcanol. Geotherm. Res.*, *150*, 98–118.

Vasco, D. W., L. R. Johnson, and N. E. Goldstein (1988), Using surface displacement and strain observations to determine deformation at depth, with an application to Long Valley caldera, California, *J. Geophys. Res.*, *93*, 3232–3242.

Waite, G. P., and R. B. Smith (2002), Seismic evidence for fluid migration accompanying subsidence of the Yellowstone caldera, *J. Geophys. Res.*, *107*(B9), 2177, doi:10.1029/2001JB000586.

Walsh, J. B., and R. W. Decker (1971), Surface deformation associated with volcanism, *J. Geophys. Res.*, *76*, 3291–3302.

Werner, C., and S. Brantley (2003), CO_2 emissions from the Yellowstone volcanic system, *Geochem. Geophys. Geosyst.*, *4*(7), 1061, doi:10.1029/2002GC000473.

Wicks, C., W. Thatcher, and D. Dzurisin (1998), Migration of fluids beneath Yellowstone Caldera inferred from satellite radar interferometry, *Science*, *282*, 458–462.

Wicks, C. W., W. Thatcher, D. Dzurisin, and J. Svarc (2006), Uplift, thermal unrest and magma intrusion at Yellowstone Caldera, *Nature*, *440*, 72–75.

Wohletz, K., L. Civetta, and G. Orsi (1999), Thermal evolution of the Phlegraean magmatic system, *J. Volcanol. Geotherm. Res.*, *91*, 381–414.

Wong, T. F., and W. F. Brace (1979), Thermal expansion of rocks: Some measurements at high pressure, *Tectonophysics*, *57*, 95–117.

Yang, X. M., P. M. Davis, and J. H. Dieterich (1988), Deformation from inflation of a dipping finite prolate spheroid in an elastic half-space as a model for volcanic stressing, *J. Geophys. Res.*, *93*, 4249–4257.

L. B. Christiansen, P. A. Hsieh, and S. Hurwitz, U.S. Geological Survey, 345 Middlefield Road, MS 439, Menlo Park, CA 94025, USA. (shaulh@usgs.gov)